

XPS for non-destructive depth profiling and 3D imaging of surface nanostructures

Shaaker Hajati · Sven Tougaard

Received: 5 September 2009 / Revised: 10 December 2009 / Accepted: 14 December 2009 / Published online: 21 January 2010
© Springer-Verlag 2010

Abstract Depth profiling of nanostructures is of high importance both technologically and fundamentally. Therefore, many different methods have been developed for determination of the depth distribution of atoms, for example ion beam (e.g. O_2^+ , Ar^+) sputtering, low-damage C_{60} cluster ion sputtering for depth profiling of organic materials, water droplet cluster ion beam depth profiling, ion-probing techniques (Rutherford backscattering spectroscopy (RBS), secondary-ion mass spectroscopy (SIMS) and glow-discharge optical emission spectroscopy (GDOES)), X-ray microanalysis using the electron probe variation technique combined with Monte Carlo calculations, angle-resolved XPS (ARXPS), and X-ray photoelectron spectroscopy (XPS) peak-shape analysis. Each of the depth profiling techniques has its own advantages and disadvantages. However, in many cases, non-destructive techniques are preferred; these include ARXPS and XPS peak-shape analysis. The former together with parallel factor analysis is suitable for giving an overall understanding of chemistry and morphology with depth. It works very well for flat surfaces but it fails for rough or nanostructured surfaces because of the shadowing effect. In the latter method shadowing effects can be avoided because only a single spectrum is used in the analysis and this may be taken at near normal emission angle. It is a rather robust means of determining atom depth distributions on the

nanoscale both for large-area XPS analysis and for imaging. We critically discuss some of the techniques mentioned above and show that both ARXPS imaging and, particularly, XPS peak-shape analysis for 3D imaging of nanostructures are very promising techniques and open a gateway for visualizing nanostructures.

Keywords Nanostructures · XPS peak-shape analysis · Depth profiling · 3D imaging

Introduction

Several methods are in use for the determination of the depth distribution of atoms. These include ion-beam (e.g. O_2^+ , Ar^+) sputtering [1, 2], low-damage C_{60} cluster ion sputtering for depth profiling of organic materials [3–5], water droplet cluster ion beam depth profiling [6], ion-probing techniques (Rutherford backscattering spectroscopy (RBS), secondary-ion mass spectroscopy (SIMS), and glow-discharge optical emission spectroscopy (GDOES)) [7], X-ray microanalysis using the electron probe variation technique combined with Monte Carlo calculations [8], angle-resolved XPS (ARXPS) [9], and X-ray photoelectron spectroscopy (XPS) peak-shape analysis [10–15]. For depths >5–10 nm, sputter depth profiling, where atoms are removed by bombardment with energetic inert gas ions (usually Ar^+), is a widespread and effective technique. It is a destructive technique and effects such as the preferential sputtering of one type of atom compared with another, intermixing, and radiation-enhanced diffusion, combine to limit the resulting depth resolution. In addition, there is the problem of the reduction of some species to lower oxidation states.

Other techniques are therefore used to achieve accurate analysis of the surface composition of the outermost few

S. Hajati (✉)
Department of Physics, Yasouj University,
Yasouj 75918-74831, Iran
e-mail: Hajati@ifk.sdu.dk
e-mail: Hajati@mail.yu.ac.ir

S. Tougaard
Department of Physics and Chemistry,
University of Southern Denmark,
5230 Odense M, Denmark

nanometers. ARXPS has been used for more than 30 years as a technique for non-destructive analysis of surface structures [9] and a facility for this analysis is available in most software. It relies on the angular dependence of the peak intensity; in other words, the greater the angle of take-off into the analyzer with respect to the surface normal, the shallower the depth z from which photoelectrons are accepted (Eq. 1). In an excellent paper by Cumpson [16], the limitations, the problems, and the accuracies that can be achieved with this method were investigated systematically from a theoretical point of view. Parallel systematic experimental investigations to determine the limitations of ARXPS have, unfortunately, not been performed except for specific systems such as SiO₂ on Si [17].

Another technique, developed by Tougaard et al. [10–15, 18, 19], relies on the fact (Figs. 1 and 5) that the inelastic background in the energy distribution of emitted electrons depends strongly on the depth concentration profile. The range of validity of this method has been studied extensively both theoretically and experimentally [15].

Angle-resolved XPS (ARXPS)

The ARXPS formalism is founded on a simple expression that relates the measured photoelectron intensity to the concentration profile, $f(z)$ viz:

$$I_A(\theta) = I_0 \int_0^{\infty} CF(z, \theta) f(z) \exp\left(-\frac{z}{\lambda \cos \theta}\right) dz \cong I_0 \int_0^{\infty} f(z) \exp\left(-\frac{z}{\lambda \cos \theta}\right) dz \quad (1)$$

where $I_0 \lambda \cos \theta$ is the intensity recorded from a reference sample with $f(z) = 1$. The factor $CF(z, \theta)$ accounts for

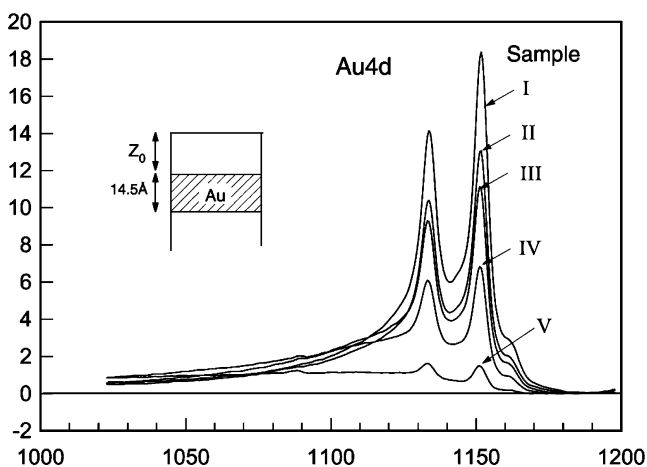


Fig. 1 Au 4d spectra measured from a thin gold layer on top of a nickel substrate (I) and after evaporation of different amounts of nickel on top (II–V). From Ref. [15]

elastic electron-scattering effects [20]. In the last expression, on the right, elastic collisions have been neglected so that $CF=1$. Elastic scattering may be important for $\theta > 60^\circ$ or if most of the detected electrons originate from layers $z > 2\lambda$. A correction for this is implemented in some software (see, e.g., Ref. [21]).

By measuring the intensity for different values of θ , the depth profile $f(z)$ can in principle be determined by comparison with Eq. 1. Several numerical procedures have been suggested [9] for inversion of Eq. 1 and thus for direct determination of $f(z)$ but they tend to be unstable and in practice a simple trial-and-error procedure is usually preferred, where $f(z)$ is changed until a good match of Eq. 1 to experiments recorded for a few values of θ is obtained. This procedure is usually executed semi-automatically by the software. Inverse Laplace transform of the angular profile $I_A(\theta)$ can give $f(z)$ but, as Cumpson describes [16], this inversion is extremely sensitive to small errors in the peak intensities.

The most serious limitation of this method is that it works only for very flat surfaces because if the surface is not flat, there is a shadowing effect for large θ . In general, the use of large values of θ cannot be avoided because $\cos \theta$ varies only slightly with θ for small θ . It is therefore necessary to include measurements at θ larger than about 50° to obtain good depth information. So for rough surfaces the interpretation of ARXPS is complicated because the angular variation of the XPS peak intensity will depend on the surface roughness. Even for ideally flat substrates, ARXPS analysis of laterally inhomogeneous surface structures grown on the surface is quite complex. The reason is that neighboring nanoclusters shadow the XPS peak intensity for large θ . The effect depends on both the shape and distribution of clusters on the surface. This is hard to correct for and ARXPS analysis may then become quite unreliable. The problem was addressed recently in detail [22–24]. For crystalline solids, measurements in high-symmetry directions should be avoided, because forward photoelectron focusing effects can lead to 20–30% variations in peak intensity which (if they are included in the analysis) lead to large errors.

Quantification of elemental depth distribution by ARXPS is however straightforward and quite accurate for perfectly flat surfaces of amorphous solids. It is applied widely to the study of thin SiO₂ layers on Si and has been shown to work very well for this particular system [17], because these surfaces can be made extremely flat. Furthermore the light elements Si and O are weak elastic scatterers, so accurate correction for elastic electron scattering is not so important. ARXPS is also useful in quantification of thin polymer films and carbonaceous contamination layers.

Traditional XPS analysis relies on XPS peak intensity assuming that the concentration in the surface region is proportional to the XPS peak intensity. There are limitations to this and it is known that more information than that typical

obtained from standard quantitative analysis can be gained by analysis of the inelastic loss structure (i.e. XPS peak-shape analysis) [14]. Figure 1 shows Au 4d spectra measured from a thin gold layer on top of a nickel substrate (I) and after evaporation of different amounts of nickel on top (II–V) [15]. The upper spectrum was taken after a small amount of Au was evaporated on to the Ni (111) surface. The spectra with progressively smaller intensity were taken after each evaporation of small amounts of Ni on top of this structure. Because of the way the samples were produced, the number of gold atoms in each of the five samples is exactly the same. Moreover, one would expect the gold to be present as a thin layer buried at increasing depths in the five samples. It is clearly seen that the peak intensity varies by a factor of 10. Therefore quantification based solely on peak intensities results in large errors. However, XPS analysis still largely relies solely on peak intensities, and so there is need for improved methods to extract the maximum information available.

Quantification based on combined analysis of peak-intensity and shape

Elaborate *QUASES-Generate* and *QUASES-Analyze*

Since 1983, methods of varying degrees of complexity for extraction of quantitative information from the large variation of the inelastic background with atom depth distribution have been suggested and will be discussed briefly here. All the information is derived from analysis of a single spectrum and is, therefore, also valid for rough surfaces when the take-off angle is close to the surface normal.

It has previously [12–15, 25–29] been shown how analysis of the inelastic peak shape in XPS spectra can be used to extract information on the in-depth distribution of electron emitters. That is, the nanostructure of the outermost surface layers can be determined. The theory and the algorithms which form the basis of the data analysis are explained in detail elsewhere [12, 14, 15, 29] and we will give a short description only.

For a given atom photoexcitation spectrum $F_i(E, \Omega_D)$ the measured spectrum $J_i(E, \Omega_D)$ from atoms with in-depth concentration profile $f_i(z)$, is given by Eq. 2 in which elastic scattering, diffraction, and surface excitation are neglected.

$$J_i(E, \Omega_D) = \frac{1}{2\pi} \int dE_0 F_i(E_0, \Omega_D) \int ds e^{is(E_0 - E)} \times \int_0^\infty dz f_i(z) \exp \left[\frac{-z}{\cos \theta} \left(\frac{1}{\lambda} - \int_0^\infty K(T) e^{-isT} dT \right) \right] \quad (2)$$

E is the kinetic energy, Ω_D the solid angle of the detector, $K(T)$ the differential inelastic scattering cross section, λ the inelastic mean free path (IMFP), and θ the angle between the surface normal and the detector.

When analyzing XPS data with this method, one seeks to determine the function $f_i(z)$ from Eq. 2. This is done in the following way. First the measured spectra are corrected for the analyzer transmission function. Next, the cascade of secondary electrons is fitted by a straight line on the high-energy side of the peak and then subtracted. Then, using the spectrum from the pure sample, $F_i(E_0)$ is determined (using Eq. 5 below) and by use of Eq. 2 a model spectrum is *generated*, assuming a specific depth profile $f_i(z)$. By comparing the model spectrum with the measured spectrum, the variable that describe the depth profile $f_i(z)$ are adjusted to give the best fit with respect to both peak shape and peak area. The analysis may be performed by the software package *QUASES-Generate* [30].

Within *QUASES-Generate* different kinds of possible in-depth concentration profiles $f_i(z)$, including buried and non-buried layer (Frank-van der Merwe), island (Vollmer–Weber), island on top of a layer (Stranski–Krastanov), and an exponential depth profile can be chosen.

Each of these profiles is defined by a set of structural parameters. An island, e.g., is described by its height and the fraction of the surface area it covers. Note that all these structures are model structures. That is, the real structure is similar to the model but not necessarily equal to it.

According to Eq. 2, $K(T)$ and λ must be known in order to evaluate $J_i(E, \Omega_D)$. The main effect of changing λ in peak-shape analysis is to change the depth scale by the same relative amount, but the type of determined nanostructure is independent of λ , as shown in several studies (see, e.g., Ref. [31]). For an island structure, the determined island coverage is thus unchanged but the island height scales directly proportional to λ . Tanuma et al. have suggested a formula to determine λ [32] If an accurate absolute calibration of the depth scale is important, it is, however, recommended to determine the effective λ from peak-shape analysis of a standard sample that is as close as possible to the composition and nanostructure of the samples being analyzed.

For most metals, their oxides, and alloys the two-parameter universal cross-section:

$$\lambda K(T) = \frac{BT}{(C + T^2)^2} \quad (3)$$

with $C=1643 eV^2$ and $B \cong 3000 eV^2$ applies with reasonable accuracy. The cross-section is normalized to unit area for $B=2C=3286 eV^2$.

For solids with a narrow plasmon structure or for insulators with band gap E_g , it has previously been shown [33] that it is more accurate to use the three-parameter universal cross-section:

$$\lambda K(T) = \theta (T - E_g) \times \frac{BT}{(C - T^2)^2 + DT^2} \quad (4)$$

where C and D are material-characteristic, $\theta(T - E_g) = 1$ for $T > E_g$ and $\theta(T - E_g) = 0$ for $T < E_g$. This may be useful for

silicon dioxide ($E_g \cong 9 \text{ eV}$) and the polymers ($E_g \cong 2\text{--}6 \text{ eV}$). The correction for band gap, where present, will only have a limited effect and only for analysis of the near-peak region.

If the analyzed peaks do not overlap in energy, it is often better to apply the so-called ‘*Tougaard-background*’ removal to determine the undistorted spectrum $F(E, \Omega_D)$. This has the advantage that the primary excitation spectrum, $F(E, \Omega_D)$, does not necessarily need to be known. The analysis relies on the formulas:

$$F(E, \Omega_D) = \frac{1}{P_1} \left[J(E, \Omega_D) - \frac{1}{2\pi} \int dE' J(E', \Omega_D) \times \int ds e^{-is(E-E')} \left(1 - \frac{P_1}{P(s)} \right) \right] \quad (5)$$

where

$$P(s) = \int f(z) e^{-\frac{z}{\cos\theta} \Sigma(s)} dz, \quad P_1 = \int_0^\infty f(z) e^{-\frac{z}{\lambda \cos\theta}} dz, \quad (6)$$

with

$$\Sigma(s) = \frac{1}{\lambda} - \int_0^\infty K(T) e^{-isT} dT \quad (7)$$

Now $P_1 = \lim_{s \rightarrow \pm\infty} P(s)$ and $1 - P_1/P(s) \rightarrow 0$ for $s \rightarrow \infty$. The function $1 - P_1/P(s)$ is therefore suitable for discrete Fourier transformation. Then the integral over s in Eq. 5 may be evaluated numerically by fast Fourier transformation. The remaining integral over E' and the integral over z may be evaluated by standard numerical methods. In this way, the original excitation spectrum corrected for inelastically scattered electrons $F(E, \Omega_D)$ is determined. Equation 5 may be used to determine either $F(E,$

$\Omega_D)$ if $f(z)$ is known (e.g., for a pure homogeneous sample) or it may be used to determine the in-depth concentration profile $f(z)$ if $F(E, \Omega_D)$ is known. Considerable information on $f(z)$ may be found even if $F(E, \Omega_D)$ is not known because, in general, one may always use the fact that $F(E, \Omega_D) \cong 0$ for all energies more than $\sim 30 \text{ eV}$ below the peak energy. For certain classes of atom depth distributions, the integration in Eq. 6 may be done analytically. References [10–15, 29, 30, 34, 35] give expressions of P_1 and $P(s)$ for different classes of depth profiles with parameters defined in Fig. 2. The expressions are tabulated in Table 1.

These equations have all been implemented in the software package *QUASES-Analyze* [30]. The method can be used for determination of λ in the nanostructures, when $f(z)$ is known by other techniques [36].

It is important to note that more accurate quantification of the nanostructure can be achieved by use of reference spectra and this is also required to determine the concentration of the elements within the nanostructure. This is done by comparing both the area and the shape of $F(E, \Omega_D)$, obtained by use of Eq. 5, with the area and shape of $F(E, \Omega_D)$ obtained from analysis of a reference sample. This gives more constraints on the fitting procedure and, as a result, the depth profiles obtained are more accurate. When possible, this is the recommended procedure for depth profiling by XPS peak-shape analysis.

The great advantage of the peak-shape analysis methods is that the accuracy is not influenced by the energy resolution and therefore the analyzer could be set at a low energy resolution to record spectra. This increases the count rates considerably and the energy step for data acquisition can also be set higher because of the resulting wider peaks. This reduces the measurement time substantially. Typical recommended values are an energy resolution of 2–5 eV (corresponding to an electron-pass energy in the analyzer of 150–300 eV) and a 0.4–1.0 eV energy step.

Fig. 2 Definition of terms for some in-depth profiles. The structures in (d), (e), and (f) give identical spectra. From Ref. [34]

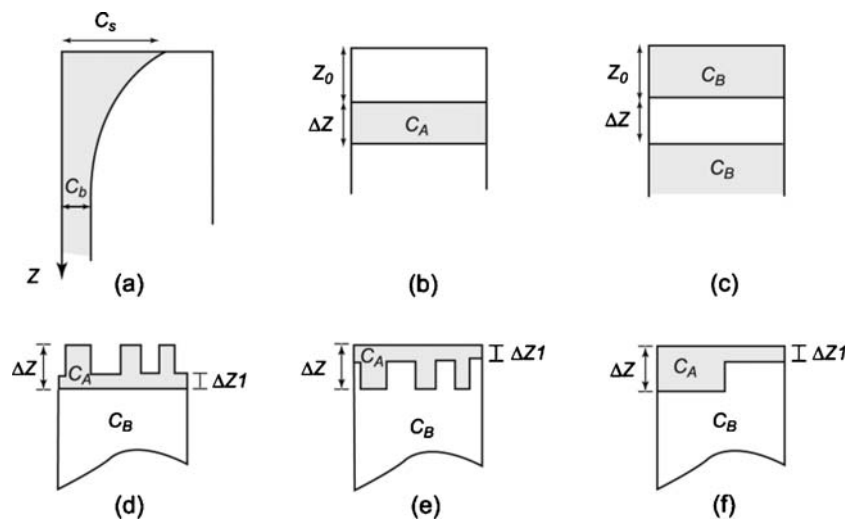


Table 1 Expressions of P_1 and $P(s)$ for different classes of depth profiles shown in Fig. 2

Depth distribution function $f(z)$		$P_1, P(s)$
$(C_s - C_b) \exp\left(-\frac{z}{L}\right) + C_b$		$P_1 = C_b \lambda_i \cos \theta + (C_s - C_b) \frac{L \lambda_i \cos \theta}{L + \lambda_i \cos \theta}$ $P(s) = C_b \frac{\cos \theta}{\Sigma(s)} + (C_s - C_b) \frac{L \cos \theta}{L \Sigma(s) + \cos \theta}$
$N \delta(z - z_0)$		$P_1 = N \exp\left(-\frac{z_0}{\lambda \cos \theta}\right)$ $P(s) = N \exp\left(-z_0 \frac{\Sigma(s)}{\cos \theta}\right)$
$f_A(z) = \begin{cases} 0 & \text{for } 0 < z < z_0 \\ C_A & \text{for } z_0 < z < z_0 + \Delta z \\ 0 & \text{for } z_0 + \Delta z < z \end{cases}$		$P_1 = C_A \lambda_i \cos \theta \cdot \exp\left(-\frac{z_0}{\lambda_i \cos \theta}\right) \left[1 - \exp\left(-\frac{\Delta z}{\lambda \cos \theta}\right)\right]$ $P(s) = C_A \frac{\cos \theta}{\Sigma(s)} \exp\left(-z_0 \frac{\Sigma(s)}{\cos \theta}\right) \left[1 - \exp\left(-\Delta z \frac{\Sigma(s)}{\cos \theta}\right)\right]$
$f_B(z) = \begin{cases} C_B & \text{for } 0 < z < z_0 \\ 0 & \text{for } z_0 < z < z_0 + \Delta z \\ C_B & \text{for } z_0 + \Delta z < z \end{cases}$		$P_1 = C_B \lambda_i \cos \theta \left\{1 - \exp\left(-\frac{z_0}{\lambda_i \cos \theta}\right)\right\} \left[1 - \exp\left(-\frac{\Delta z}{\lambda \cos \theta}\right)\right]\right\}$ $P(s) = C_B \frac{\cos \theta}{\Sigma(s)} \left\{1 - \exp\left(-z_0 \frac{\Sigma(s)}{\cos \theta}\right)\right\} \left[1 - \exp\left(-\Delta z \frac{\Sigma(s)}{\cos \theta}\right)\right]\right\}$
$f_A(z) = \begin{cases} C_A & \text{for } 0 < z < \Delta z_1 \\ f_1 C_A & \text{for } \Delta z_1 < z < \Delta z \\ 0 & \text{for } \Delta z < z \end{cases}$		$P_1 = C_A \lambda_i \cos \theta \left\{1 - (1 - f_1) \exp\left(-\frac{\Delta z_1}{\lambda_i \cos \theta}\right) - f_1 \exp\left(-\frac{\Delta z_1}{\lambda_i \cos \theta}\right)\right\}$ $P(s) = C_A \frac{\cos \theta}{\Sigma(s)} \left\{1 - (1 - f_1) \exp\left(-\Delta z_1 \frac{\Sigma(s)}{\cos \theta}\right) - f_1 \exp\left(-\Delta z_1 \frac{\Sigma(s)}{\cos \theta}\right)\right\}$
$f_B(z) = \begin{cases} 0 & \text{for } 0 < z < \Delta z_1 \\ (1 - f_1) C_B & \text{for } \Delta z_1 < z < \Delta z \\ C_B & \text{for } \Delta z < z \end{cases}$		$P_1 = C_B \lambda \cos \theta \left\{(1 - f_1) \exp\left(-\frac{\Delta z_1}{\lambda_i \cos \theta}\right) - f_1 \exp\left(-\frac{\Delta z_1}{\lambda_i \cos \theta}\right)\right\}$ $P(s) = C_B \frac{\cos \theta}{\Sigma(s)} \left\{(1 - f_1) \exp\left(-\Delta z_1 \frac{\Sigma(s)}{\cos \theta}\right) - f_1 \exp\left(-\Delta z_1 \frac{\Sigma(s)}{\cos \theta}\right)\right\}$

Shadowing effects for rough surfaces and increased importance of elastic scattering effects and surface excitations which might cause some errors for large emission angles may, to a large extent, be avoided in the peak-shape analysis method. To this end, it is therefore recommended to measure the spectra at an emission angle not too far (preferably $<45^\circ$) from the surface normal. If the sample is crystalline, one should use large analyzer acceptance angles and avoid angles of high crystalline symmetry, because forward focusing effects are largest in these directions.

The XPS-peak-shape method is non-destructive and therefore also allows one to study the change in surface composition during surface treatment as, e.g., in chemical reactions and gradual annealing. It has been applied by many research groups in the study of a wide range of systems and physical phenomena, including growth mechanisms and nanostructures of metal/metal [25–27, 37–43], metal/silicon [28, 44, 45], metal/germanium [45], germanium/silicon [46–49], $\text{In}_x\text{Ga}_{1-x}\text{As}$ films [50], amorphous $\text{a-Si}_{1-x}\text{C}_x\text{:H}$ alloys [51], polymer systems [52–54], metal-nanoparticle/HOPG [55], metal-nanoparticle/ Al_2O_3 [56], metal-nanoparticle/polymer systems [57], C-segregation on Ni [41], metal oxide growth [15, 58–64], SiO_2 films [31, 65], nucleation of ZnTe on As-terminated Si [66], and the depth excitation function in electron stimulated AES [67, 68]. Some of these were reviewed in Ref. [15]. Several tests on the validity of the method have also been done by comparing with other techniques, for example AFM [43, 47–49, 54], RBS [31, 37, 48], ISS [63], ellipsometry [31], ARXPS [31, 53], RBS [31, 37], quartz-crystal microbalance (QCM) [25, 38, 42, 57], RHEED [66], TEM [57], XTEM [42] and use of Synchrotron radiation with varying photon energy [40, 69, 70].

Applications of QUASES-Generate

To use Eqs. 5–7, minimal interference of neighboring lines across a wide spectral range is required. This could be a limitation for that method. However, *QUASES-Generate* has been used to handle this limitation. Simonsen et al. successfully used *QUASES-Generate* for depth profiling the nanostructure of Ge deposited on Si(001) [46]. Graat et al. [58, 71] used it to determine the depth distributions of different iron oxide structures where overlapping peaks are present. *QUASES-Generate* was also applied by Grosvenor et al. [59, 60]. Jussila et al. investigated the morphology and composition of nanoscale surface oxides on Fe-20Cr-18Ni{111} austenitic stainless steel [72] and the initial stages of surface oxidation of Fe-17Cr (ferritic stainless steel) [73]. Schleberger [74] used the method to investigate amorphous Fe/Ge/Fe structure and to see to what extent the interface between the metal and the semiconductor is sharp.

Graat et al. [58] evaluated the composition and thickness of thin iron oxide films on polycrystalline pure iron from Fe 2p XPS spectra. To this end, the experimental spectra were reconstructed from reference spectra of the constituents Fe^0 , Fe^{2+} , and Fe^{3+} (Fig. 3). The background contributions in the spectra owing to inelastic scattering of signal electrons were calculated from the depth distributions of these constituents and their reference spectra. In the reconstruction procedure the film thickness and the concentrations of Fe^{2+} and Fe^{3+} in the oxide film were used as fit parameters. As mentioned above, the contribution of a species i (including its background), $J_i(E, \Omega_D)$, to an overall spectrum can be calculated from the corresponding intrinsic spectrum, $F_i(E, \Omega_D)$, by use of Eq. 2. Note that i stands for Fe^0 , Fe^{2+} , and Fe^{3+} . To calculate $J_i(E, \Omega_D)$ the corresponding depth distribution, $f_i(z)$ and λ and $K(T)$ have to be known. (Note that in general λ and $K(T)$ depend on the composition-depth profile of the sample). Usually, $f_i(z)$ (and thus λ and $K(T)$) is not known. Then, a first guess for $f_i(z)$ of each of the species i can be made and the corresponding spectral contributions are calculated from the intrinsic spectrum, $F_i(E, \Omega_D)$, by use of Eq. 2. After summation over all spectral contributions one obtains the reconstructed spectrum $J_i(E, \Omega_D)$ which can be compared with the measured spectrum, $J(E)$, to obtain the squared difference χ^2

$$\chi^2 = \int_{E=0}^{\infty} \left[J(E) - \sum_i J_i(E) \right]^2 dE \quad (8)$$

Then, optimum depth distributions for the species i can be found by modification of the estimates for $f_i(z)$ (and related λ and $K(T)$), while minimizing χ^2 .

In a similar recent analysis by Jussila et al. [75], *QUASES-Generate* was used to study in situ the initial oxidation stages of three FeCrNi-alloys. This analysis gave

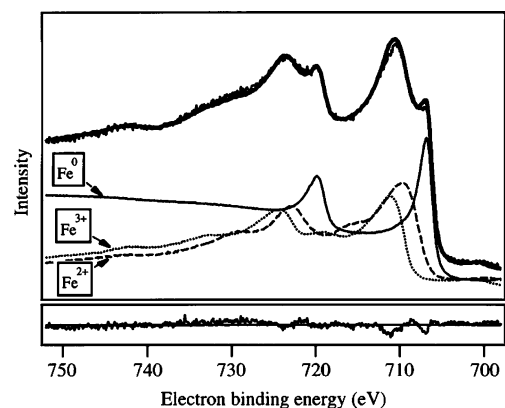


Fig. 3 Reconstruction of experimental Fe 2p spectra of sputter-cleaned $\alpha\text{-Fe}$: oxidized for 30 min at 373 K in O_2 at 3×10^{-5} Pa. The individual contributions of Fe^0 , Fe^{2+} , and Fe^{3+} are shown, and the experimental and reconstructed spectra. Lower parts show the difference between the experimental and reconstructed spectrum on the same scale as the spectra. From Ref. [58]

quite detailed information on the depth distribution of nanostructures of Fe and Cr oxides after O₂ exposure.

Applications of QUASES-Analyze

As mentioned above, peak-shape analysis using the *QUASES* software package has been successfully used in the study of a wide range of system and physical phenomena [15, 25–28, 31, 37–45, 47–56, 61–68]. In a recent XPS peak-shape analysis by Kisand et al. [76] the morphology and thickness of ultrathin films of KCl on Copper were estimated.

Schleberger et al. investigated amorphous Fe/Si and Fe/Ge nanostructures by analyzing wide range spectra of the Fe3*p* and Fe2*p* from the overlayer and Si*KLL* and Ge*LMM* from the substrate [45]. It was shown that XPS peak-shape analysis could be used to determine the morphology of surface nanostructures by analyzing signals from either overlayer or substrate. This is an *advantage* of the method, i.e., even in case acquiring a spectrum with a good signal-to-noise ratio is possible from only the substrate and not from the overlayer it is still possible to characterize the overlayer by analyzing spectrum from the substrate.

Interface effects in the Ni2*p* XPS spectra of NiO thin films grown on different oxide substrates, namely SiO₂, Al₂O₃ and MgO, were quantitatively studied by Preda et al. [77] by using XPS peak-shape analysis.

Recently, Gonzalez-Elipe et al. have used the method to describe the size and shape of the nuclei of several oxides grown on different substrates [63, 78–84], e.g. supported zirconia nanoparticles on SiO₂, Y₂O₃, and CeO₂ [85]. The characterization of these nuclei is important because their size, shape, and dispersion degree on the surface are critical for the control of the microstructure of the thin films. The interest of this type of analysis is not limited to thin-film nucleation as in the example of supported zirconia nanoparticles, but can be of interest for other situations where knowledge of the shape and size of supported particles may be important (e.g., catalysts, supported nanoparticles, etc.). In this regard, it is interesting to recall that in many experimental situations it is not possible to assess the particle size and shape of deposited nanoparticles by means of classical microscopy methods. This is the case when, with materials with a high electron density or high surface roughness, electron microscopy or atomic force microscopy fails to differentiate the structures of a support from those of the supported nanoparticles. It is believed that in these cases XPS peak-shape analysis can be very useful for a morphological characterization of supported nanoparticles [85].

Wetting properties of poly(ethylene terephthalate) (PET) and low-density polyethylene polymers were investigated by the method after treatment with a microwave (MW) plasma discharge at low pressure and a dielectric barrier discharge at atmospheric pressure. The oxygen distribution

between the topmost surface layer and the bulk was obtained [86] by non-destructive XPS peak-shape analysis.

In all of these studies, different classes of depth profiles illustrated in Fig. 2 were used. Recently Hajati et al. [57] applied the method to study how gold nanoclusters grow, diffuse and distribute in polystyrene as a function of both cluster size and temperature in the range from below to above the glass transition temperature of the polymer. The study was done by considering the profile shown in Fig. 2f and setting $\Delta Z_1=0$. To make it applicable to determination of the size and density of Au nanoclusters, each spherical nanocluster (with diameter $2R$ and surface coverage f_1) was divided into nine coaxial cylindrical shells with the same surface coverage and different height. The size ($2R$) of the nanoclusters was then adjusted to subtract the inelastic background from the measured spectrum (Fig. 4) and the surface coverage was adjusted to fit the background subtracted spectrum to the reference spectrum $F(E, \Omega_D)$.

In this way, the size and density of Au nanoclusters were determined for four different amounts of gold deposition.

It is noted here that although in Ref. [57] the shape of the nanocluster was modeled as a sphere using multiple islands of varying height, the analysis is not sensitive enough to discriminate between a sphere and a cube as long as the volume is identical (this is actually also mentioned in Ref. [57] but is worth stressing in this context because the figures in Ref. [57] might give this impression). With peak-shape analysis, only the three primary properties that describe the main characteristics of the nanostructure are determined with high accuracy, see also Ref. [15]. In this case these three parameters were the gold coverage, height, and concentration. All information can, however, be deduced from the determined island height and coverage. Thus, taking the height as the nanocluster diameter, the nanocluster density can readily be calculated from the coverage.

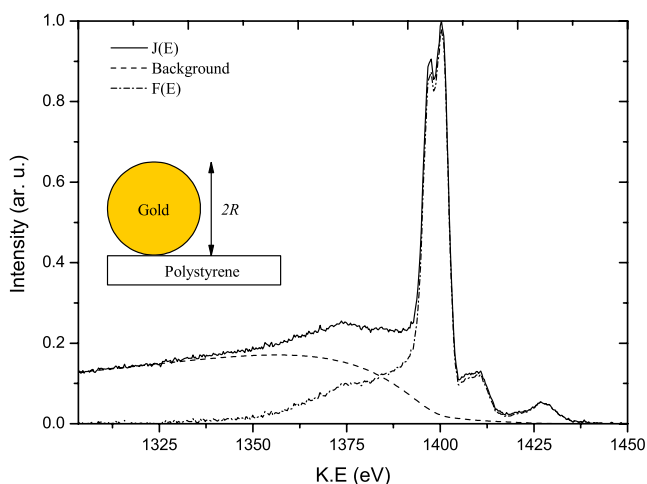


Fig. 4 Analyzed Au 4*f* spectrum for 24 Å gold at room temperature. From Ref. [57]

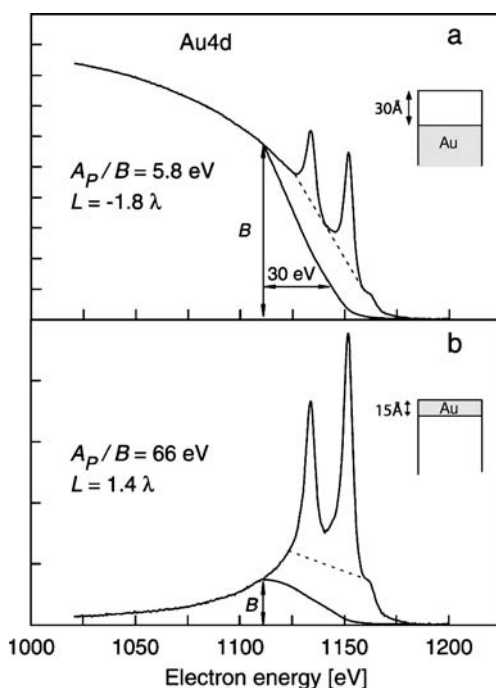


Fig. 5 Two examples of the application of the A_p/B and decay length (L) methods. The two model spectra were calculated for (a) a gold substrate covered with a 3.0 nm overlayer and (b) a 1.5 nm gold film on top of a substrate. $\lambda = 1.5$ nm in both cases. From Ref. [34]

The results obtained are in excellent agreement with QCM and TEM. The authors also successfully studied the gradual embedding of the Au clusters as the temperature was raised. The method can thus give this detailed quantitative information on such a metalized polymer without the need for any other complimentary and time-consuming technique such as AFM, TEM, and XTEM. It is also important to note that this information is obtained very quickly from analysis of a single XPS spectrum and that the changes can be followed in almost real time by sequentially measuring the XPS as the growth or temperature-induced effects happen.

Peak area-to-background ratio A_p/B

The simplest quantitative description of the variation in peak shape and background with depth is to take the ratio

of the peak area A_p to the increase in background B at a chosen energy below the peak energy. This ratio is very sensitive to the in-depth distribution because A_p and B vary in opposite directions as a function of the depths of the atoms in a solid. For homogeneous distribution of atoms it has been shown that this ratio, D_0 , is fairly constant (~ 23 eV), independently of material and peak energy. Substantial deviations from this value can then be used to estimate the depth distribution of atoms [10, 87].

The algorithm can be defined from Fig. 5. A_p is the peak area (of the doublet in this case) determined after a linear background has been subtracted (dashed line) from the measured spectrum. The upper energy point to be chosen for the straight line background is taken to be the energy at which the spectral intensity is 10% of that at the peak energy, while the low energy point at the other end of the straight line is defined as being at the same distance below the peak energy as the high energy point is above it [10]. B is the increase in intensity measured 30 eV below the peak energy. (In the case, as here, of a doublet peak, the geometrical weighted centroid of the peak structure is used as reference energy). A quick estimate of the in-depth distribution of atoms can then be found from the rules in Table 2. For a given system, the method may be fine-tuned by calibrating D_0 against A_p/B determined from the analysis of a sample known to have a homogeneous atom distribution. An example of its application is also shown in Fig. 5, where the values A_p/B are seen to be consistent with the rules in Table 2. Other examples of its practical application by Johansson et al. may be found in Refs. [88, 89]. Recently, Perring et al. used it to determine the depth distribution of F atoms in an assembly of organic monolayers on polydicyclopentadiene [90] and it was also used by Walton et al. to obtain images of oxide film thickness (SiO_x/Si) after noise reduction by principal-component analysis [91].

3D XPS nano-imaging

As seen in the section “*Elaborate QUASES-Generate and QUASES-Analyze*”, the elaborated method for XPS peak-shape analysis is quite accurate and rather easy to apply. However, it requires operator interaction, and is therefore

Table 2 Rules for estimating the depth profile from A_p/B . From Refs. [10, 87]

A_p/B	Depth distribution
~ 23 eV	Uniform
> 30 eV	Surface localized
< 20 eV	Subsurface localized
If the same peak from two samples has the values $D_1 = (A_p/B)_1$ and $D_2 = (A_p/B)_2$ then:	
if $30 \text{ eV} < D_1 < D_2$	Atoms are surface localized in both samples and are at shallower depths in sample 2 than in sample 1
if $D_1 < D_2 < 20 \text{ eV}$	Atoms are primarily in the bulk of both samples and at deeper depths in sample 1 than in sample 2

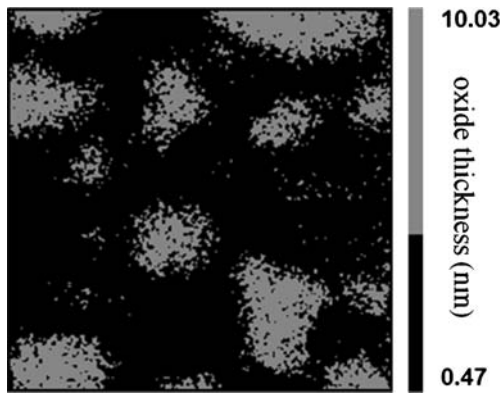
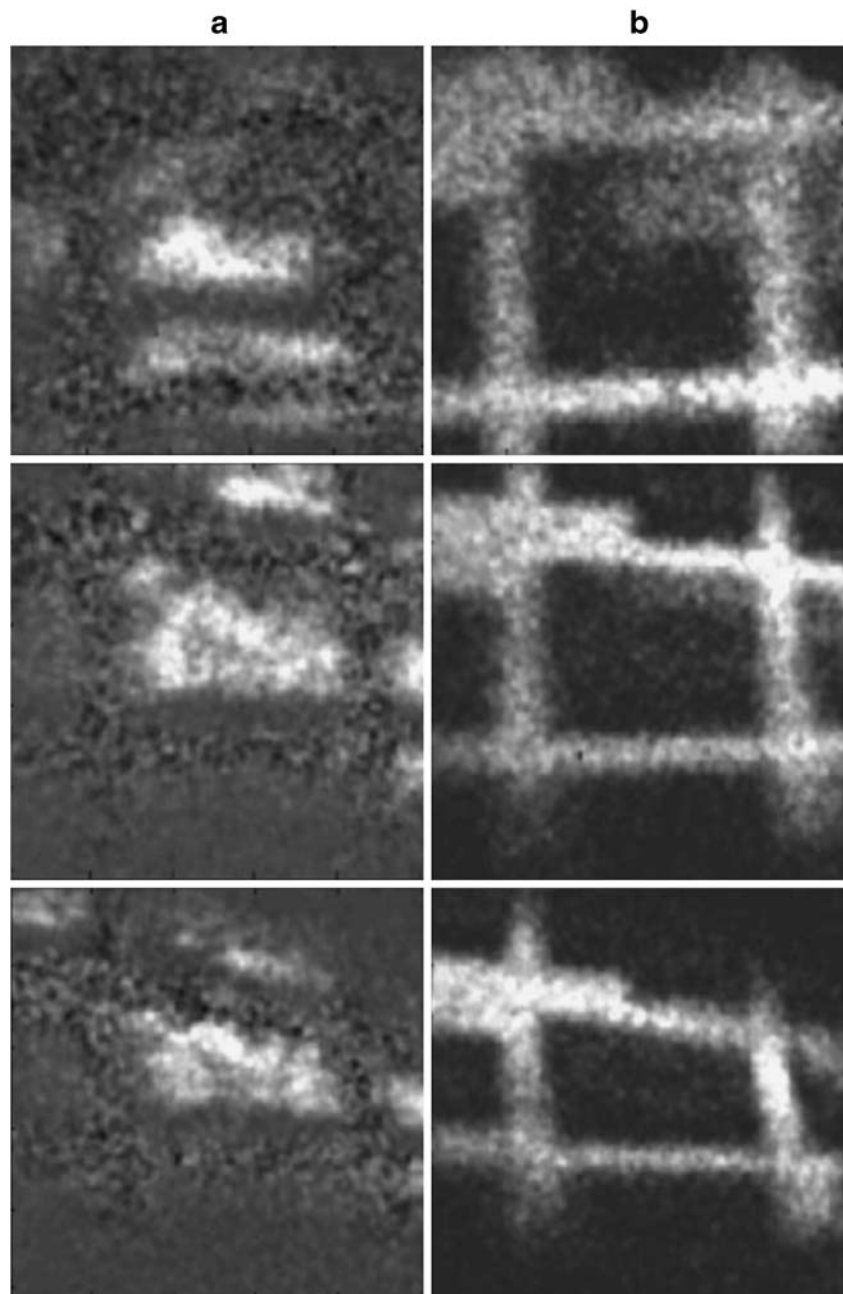


Fig. 6 Image of oxide thickness from GeO_2/Ge . From Ref. [97]

Fig. 7 The $700\ \mu\text{m} \times 700\ \mu\text{m}$ Cl 2p (a) and associated background (b) images for 90° (top), 60° (middle), and 30° (bottom) TOAs. Background images reflect the changes in geometry which occur when tilting the sample. From Ref. [99]



not practical for XPS imaging where thousands of spectra must be analyzed.

XPS imaging has become of increasing interest in the past decade because of improvements in both data acquisition and subsequent processing. In particular, the applicability of this technique for determination of accurate depth distributions on the nanometer scale is highly important. It is known that more information than that typically obtained from standard quantitative analysis can be gained by XPS peak-shape analysis [14] (Fig. 1). Thus XPS peak-shape analysis gives the depth distribution of atoms, the surface concentration, and the amount of substance (AOS) of a given element in the outermost few

nanometers [14]. However, XPS imaging still largely relies solely on peak intensities, and so there is a need for improved methods to extract the maximum information available. The current methods of XPS imaging were reviewed by Artyushkova [92] with a focus on combination of ARXPS and mapping and multivariate analysis [93–96] of ARXPS data.

Recently, Smith et al. obtained images of thickness of the moisture-induced corrosion of an evaporated germanium film, GeO_2/Ge (Fig. 6), [97] by using:

$$d = L \cos \theta \cdot \ln \left(1 + R_{\text{exp}}/R_0 \right) \quad (9)$$

where L is the virtually identical attenuation length of the Ge 3d electrons from the oxide and underlying metal (within the oxide), θ is the emission angle from the surface normal, R_{exp} is the measured Ge 3d intensity ratio $I(\text{GeO}_2)/I(\text{Ge})$ from the sample, and R_0 is the same ratio for signals from infinite solids with flat surfaces measured under identical conditions. Equation 9 follows from Eq. 1 when it is assumed that the overlayer forms a complete layer of uniform thickness.

Equation 9 was also used for imaging of SiO_x/Si [98]. A limitation of this method is that it applies only for oxides and it is assumed that the oxidized layer is uniform and covers the complete surface. This approach is therefore mostly useful for obtaining thicknesses of overlayers and does not provide the distribution of chemical phases in the 3D volume of the material.

Artyushkova and Fulghum have developed a technique and applied it to ARXPS imaging [99] of heterogeneous polymer blends of PVC and PMMA. The experimental procedure for acquiring angle-resolved images was established using a Cu grid as a marker for location of the analysis area. Figure 7 shows the Cl 2p and associated background images for take-off angles (TOA) of 90° , 60° , and 30° . Cl 2p images, having the highest contrast level, are used as representative of the PVC-enriched phases. The final result will thus be a visualization of the 3D

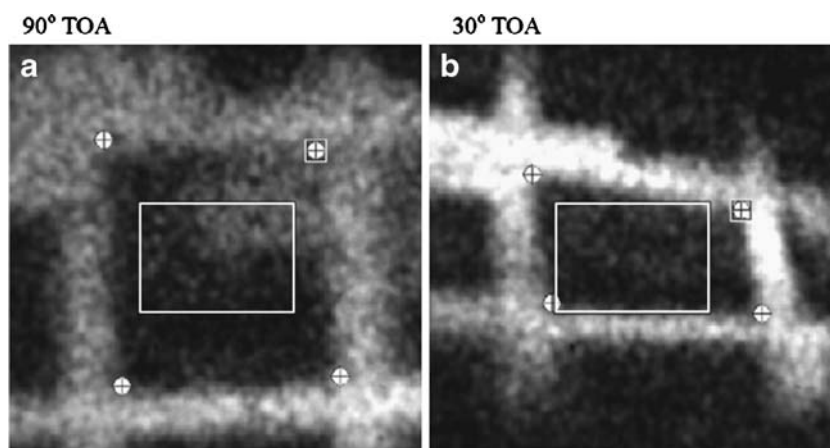
morphology of the PVC-enriched areas of the blend. For a two-component system, this is a full representation of the sample, as the PMMA-enriched phase will be an exact inverse of the PVC-enriched phase. Background images for the Cl 2p main peak show a distinct outline of the Cu grid. The spatial transformations resulting from tilting the sample are evident in these images. The features in the images change shape, and there is a loss of focus at the top and bottom of the images. The current imaging photoelectron spectrometers have a smaller focal depth of field in image acquisition mode than in spectroscopy mode.

Intensities therefore may be unusually high or low in areas of the image that are not in focus. The images must be brought to the same spatial coordinates by image registration. Artyushkova and Fulghum performed this [99] by converting an image from one coordinate system to another by using a group of control points (GCPs) (Fig. 8) and the transformation equations required. As shown in Fig. 8, the corners of the Cu grid are selected for these four points. Note that all limitations of large-area ARXPS mentioned in the section “*Angle resolved XPS (ARXPS)*” hold for the ARXPS imaging technique proposed by Artyushkova and Fulghum. However it is a promising technique for making a 3D image of nanostructures, particularly where flat surfaces and polymers are analyzed.

Another XPS-imaging technique, uses the method in the section “*Peak area-to-background ratio A_p/B* ”, i.e. the ratios of peak area to background signal at 30 eV below peak energy [87], for each pixel is used to get information on the depth profile. Walton and Fairley applied this to get images of film thickness for the SiO_x/Si system, after noise reduction by principal-component analysis [91]. Noise reduction is important because this approach uses the value of the background intensity at a single point, 30 eV below peak energy, which is sensitive to the noise.

As discussed in the section “*Quantification based on combined analysis of peak-intensity and shape*”, detailed

Fig. 8 Selection of ground control points (GCPs) from (a) 90° TOA and (b) 30° TOA background Cl 2p images. Projective transformation requires four GCPs. The corners of the grid are selected for these four points. From Ref. [99]



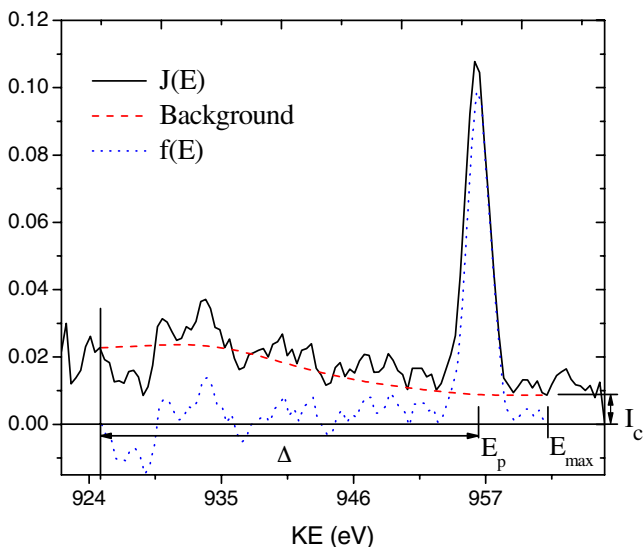


Fig. 9 Definition of quantities used in this section (a typical O 1 s spectrum)

analysis of XPS peak shape can give very detailed information on the depth distribution. However this requires manual analysis of the spectrum from each pixel and is not well suited for imaging where thousands of spectra must be analyzed. Recently, Tougaard proposed a simplified and robust algorithm [100] to characterize the outermost three inelastic electron mean-free paths (λ) of the sample. In this method, the background is adjusted to match the spectrum at a single energy below the peak which makes it suitable for automatic data processing [100]. The validity was tested for large-area ($\sim 5 \times 5 \text{ mm}^2$) XPS taken from different nanostructures and it was found that the AOS within the outermost 3λ ($AOS_{3\lambda}$) determined using this simplified method deviates typically less than 10% from the results obtained with other more elaborate techniques, and that surface, bulk, and homogeneous depth distributions [101] can clearly be distinguished.

Here, we summarize the algorithm derived in Ref. [100]. Let $J(E)$ denote the energy distribution of emitted electrons.

The peak structure of interest is centered around the energy E_p and the high energy end of the spectrum E_{\max} is chosen a few eV above the peak structure (Fig. 9). All energies are in kinetic energy.

Depending on the material studied, we use either the two-parameter universal cross section from Eq. 3 with adjustable parameter C or the three-parameter universal cross section from Eq. 4 with adjustable parameters C and D to match the cross section characteristic of the solid. The first step is to correct for inelastic electron scattering and to calculate the background-subtracted spectrum, $f(E)$, using either Eqs. 10 or 11 (for the detailed basis of the algorithm see Ref. [100])

$$f(E) = J(E) - B_1 \int_E^{E_{\max}} J(E') \frac{E' - E}{[C + (E' - E)^2]^2} dE' \tag{10}$$

$$f(E) = J(E) - B_1 \int_E^{E_{\max}} J(E') \frac{E' - E}{[C - (E' - E)^2]^2 + D(E' - E)^2} dE' \tag{11}$$

for the energy range $E_p - \Delta < E < E_{\max}$, where Δ is chosen between 20 and 40 eV (Fig. 9). It has been shown that the final result of the analysis does not depend significantly on the exact value of Δ as long as it is in this range [101]. B_1 is adjusted such that $f(E_p - \Delta) = 0$. Here we have used $\Delta = 30$ eV.

From $f(E)$ the peak area is determined:

$$A_p = \int_{E_p - \Delta}^{E_{\max}} f(E) dE \tag{12}$$

To make an absolute determination of the AOS, it is necessary to calibrate the instrument. This may be done by analysis of the spectrum for the same XPS peak from a solid with homogeneous distribution of atoms of density c_H . Let B_0 and A_p^H denote the B_1 and A_p values obtained

Table 3 Rules for estimating the depth profile from L^* [100, 101] (see Section III.B in Ref. [101] for experimental proof of the rules)

L^*	Depth distribution
Rule I $0 < L^* \lesssim 1$	Most atoms are at depths $< \lambda$ (surface region)
$-1 \lesssim L^* < 0$	Most atoms are at depths $> \lambda$ (bulk region)
$2 \lesssim L^* $	Approximately constant (homogeneous region)
If the same peak from two samples, in this case two pixels, have values L^*_1 and L^*_2 , then:	
Rule II $0 < L^*_1 < L^*_2$	Atoms are surface localized in both samples and the atoms are at more shallow depth in sample 1 than in sample 2
Rule III $L^*_1 < L^*_2 < 0$	Atoms are primarily in the bulk of both samples and at deeper depth in sample 2 than in sample 1

from analysis by either Eqs. 10 or 11 and 12, respectively, of the spectrum from the homogeneous reference.

Now calculate

$$L^* = L/3 \lambda = \frac{B_1}{B_0 - B_1} (\cos \theta)/3 \quad (13)$$

where θ is the angle of emission with respect to the surface normal. Note that in the algorithm, all kinds of depth distributions are approximated to an exponentially varying function with decay constant $1/L$. This means that the value of L and therefore the value of L^* gives a rough indication of the in-depth distribution of atoms. In practice, it has been found that the rules in Table 3 apply [100, 101].

Furthermore, the amount of substance within the outermost 3λ is [100]:

$$AOS^* = AOS/3\lambda = \frac{L^* + (\cos \theta)/3}{1 - e^{-\frac{3}{\cos \theta} + \frac{1}{L^*}}} (1 - e^{-1/L^*}) \frac{A_p}{A_p^H} \quad (14)$$

where we have set $c_H=1$ and consequently AOS^* is the amount of atoms within depths 3λ relative to the amount of atoms in the pure samples. This method, however, is limited to providing the distribution of elements and not the chemical state of the atoms. Another limitation is that it requires non-overlapping peaks (this is usually not a big problem in polymers because there are so few peaks). Although overlapping peaks can be handled with *QUASES-Generate* this analysis is more involved and probably not suitable for imaging.

Recently, Hajati et al. [102–104] used the above mentioned algorithm (Eqs. 10–14) to investigate its practical applicability for 3D XPS imaging of nanostructures. In Ref. [102] it was tested for a *qualitative* study of plasma patterned propanal on Teflon substrate. It was shown that the algorithm can successfully categorize the approximate depth distributions of atoms. Here we present a 3D image of propanal (Fig. 10), which has not been published previously.

In Ref. [103], a *quantitative* test of the algorithm's ability is also demonstrated—production of images of Ag taken from a series of samples with increasing thicknesses of plasma patterned octadiene (2, 4, 6, and 8 nm) on Ag substrates. The images obtained of the amount of silver atoms in the outermost few nanometers of the samples were



Fig. 10 3D image of patterned propanal on Teflon substrate



Fig. 11 3D image of patterned octadiene on Ag substrate

in good agreement with the nominal thicknesses. For a given sample, different categories of depth distributions of atoms were distinguished, which clearly proves the suitability of the method for quantitative and nondestructive 3D characterization of nanostructures. The results of the detailed analysis can be found in Ref. [103]. Here we show the 3D image of Octadiene with 6 nm nominal thickness in Fig. 11. This has not been published previously.

In Ref. [104], methods to reduce the effect of spectral noise were studied. It was found that principal-components analysis (PCA) when applied to the full set of spectra from all pixels gives a substantial improvement in the signal-to-noise level of the spectra. This is important because data acquisition time is a limiting factor in imaging. More specifically, images of thermally patterned oxidized silicon made through a photolithographic mask were produced for different depth distributions of atoms. It was shown that images of the Si, O, and C atoms were complementary. Results of the detailed analysis can be found in Ref. [104]. Here we show in Fig. 12 a 3D image of islands of SiO_2 ; this has not been published previously.

These experiments show that the algorithm [100] is rather robust and quantitative and that it seems to have a great potential for non-destructive 3D imaging of the chemical composition of nanostructures.

Summary and outlook

Depth profiling of nanostructures is of high importance both technologically and fundamentally. Therefore, many different methods have been developed for determination of the depth distribution of atoms; these include ion-beam (e.g. O_2^+ , Ar^+) sputtering, low-damage C_{60} cluster-ion sputtering for depth profiling of organic materials, water droplet cluster ion beam depth profiling, ion-probing



Fig. 12 3D image of patterned thermally oxidized silicon

techniques (Rutherford backscattering spectroscopy (RBS), secondary-ion mass spectroscopy (SIMS), and glow-discharge optical emission spectroscopy (GDOES)), X-ray microanalysis using the electron probe variation technique combined with Monte Carlo calculations, XPS in combination with sputtering, angle-resolved XPS (ARXPS), and X-ray photoelectron spectroscopy (XPS) peak-shape analysis. In this paper we have focused on non-destructive methods based on XPS. Each of the depth profiling techniques has its own advantages and disadvantages. However, in many cases, non-destructive techniques are preferred which includes ARXPS and XPS peak-shape analysis. The former together with parallel factor analysis is suitable for giving an overall understanding of chemistry and morphology with depth. It worked well for flat surfaces but, because of the shadowing effect, it is unreliable for rough samples and for nanostructures on an otherwise flat substrate. The latter enables robust determination of atom depth distributions on the nanoscale both for large-area XPS analysis and for imaging. Its main limitation is that analysis is complex (although still possible) when it is not possible to find a peak that is free from interfering peaks from other atoms in an energy range from at least ~ 50 eV below to ~ 20 eV above the peak.

We have critically discussed some of the mentioned techniques and show that both ARXPS imaging and, particularly, XPS peak-shape analysis for 3D imaging of nanostructures are very promising techniques and open a gateway for visualizing nanostructures. The XPS peak-shape analysis method, however, is limited to providing distribution of elements and not chemical species. It also requires non-overlapping peaks (usually not a big problem in polymers because there are so few peaks). Overlapping peaks can be handled with *QUASES-Generate* but this is a more involved analysis and will probably not be useful for imaging. We have shown that the depth resolution of the XPS peak-shape analysis technique is sub-nanometer. However, the spatial resolution is limited by the design of the XPS imaging instruments and is, at best, ~ 150 nm (Omicron) [105], at the time of writing. Third-generation synchrotron beam lines give spatial resolution of about 20 nm. In future work, it is worth using the benefit of these beam lines for visualization of nanostructures. With such high resolution, the acquired spectra are expected to be noisier than the spectra for which we have already tested the technique. However a noise reduction procedure such as PCA is found to be very efficient.

There are impartial reasons for low involvement of XPS in investigations of biologically related objects. First, organic chemistry samples often exhibit high vapor pressure and therefore, degas badly in vacuum. This is not compatible with the XPS technique. Second, X-rays might cause radioactive damage of a sample. However, with the

new improved processes for, e.g., immobilization of bio-materials, XPS is becoming of more interest to characterize biological surfaces [106, 107], providing critical information on, e.g., coverage of the surface of the materials. Therefore, our technique with its capability for 3D imaging of in-depth distribution of atoms could make a gateway for investigating biomaterials to give an answer to open questions in, e.g., tissue engineering and DNA-modified surfaces required for microarray and biosensor applications.

References

- Jiang ZX, Alkemade PFA (1999) *Surf Interface Anal* 27:125–131
- Kang HJ, Moon DW, Lee HI (2009) *J Surf Anal* 15:216–219
- Sostarecz AG, McQuaw CM, Wucher A, Winograd N (2004) *Anal Chem* 76:6651
- Kozole J, Szakal C, Kurczy M, Winograd N (2006) *Appl Surf Sci* 252:6789
- Conlan XA, Gilmore IS, Henderson A, Lockyer NP, Vickerman JC (2006) *Appl Surf Sci* 252:6562–6565
- Sakai Y, Iijima Y, Takaishi R, Asakawa D, Hiraoka K (2008) *J Surf Anal* 14:466
- Galindo RE, Gago R, Lousa A, Albella JM (2009) *Trends Anal Chem* 28:494–505
- Bakaleinikov LA, Domrachova YV, Kolesnikova EV, Zamoryanskaya MV, Popova TB, Flegontova EY (2009) *Semiconductors* 43:544–549
- Cumpson PJ (2003) In: Briggs D, Grant JT (eds) *Surface analysis by Auger and X-ray photoelectron spectroscopy*. IM-Publications, Chichester, pp 651–675
- Tougaard S (1985) *Surf Sci* 162:875–885
- Tougaard S (1987) *J Vac Sci Technol A* 5:1230–1234
- Tougaard S (1988) *Surf Interface Anal* 11:453–472
- Tougaard S, Hansen HS (1989) *Surf Interface Anal* 14:730–738
- Tougaard S (1996) *J Vac Sci Technol A* 14:1415–1423
- Tougaard S (1998) *Surf Interface Anal* 26:249–269
- Cumpson PJ (1995) *J Electron Spectrosc Relat Phenom* 73:25–52
- Seah MP (2004) *J Vac Sci Technol A* 22:1564–1571
- Tanuma S, Powell CJ, Penn DR (1993) *Surf Interface Anal* 21:165–176
- Tanuma S, Powell CJ, Penn DR (2003) *Surf Interface Anal* 35:268–275
- Jablonski A, Tougaard S (1998) *Surf Interface Anal* 26:374–385
- Lassen T, Tougaard S [Online] Ver 1.1, (2002–2005). *QUASES-ARXPS*; software for quantitative XPS/AES of surface nanostructures by ARXPS. www.quases.com
- Oswald S, Oswald F (2008) *Surf Interface Anal* 40:700–705
- Kappen P, Reihs K, Seidel C, Voertz M, Fuchs H (2000) *Surf Sci* 465:40
- Martin-Concepcion AI, Yubero F, Espinos JP, Tougaard S (2004) *Surf Interface Anal* 36:788–792
- Hansen HS, Jansson C, Tougaard S (1992) *J Vac Sci Technol A* 10:2938–2944
- Tougaard S, Hansen HS (1990) *Surf Sci* 236:271
- Tougaard S, Hansen HS, Neumann M (1991) *Surf Sci* 244:125–134
- Schleberger M, Fujita D, Scharfschwerdt C, Tougaard S (1995) *Surf Sci* 331/333:942–947
- Tougaard S (1996) *Appl Surf Sci* 100:1–10

30. Tougaard S [Online] Ver. 5.1, QUASES, (1994–2005). Software package for quantitative XPS/AES of surface nanostructures by peak shape analysis. www.quases.com
31. Semak BS, Van der Marel C, Tougaard S (2002) *Surf Interface Anal* 33:238–244
32. Tanuma S, Powell CJ, Penn DR (1991) *Surf Interface Anal* 17:911
33. Tougaard S (1997) *Surf Interface Anal* 25:137–155
34. Tougaard S (2003) In: Briggs D, Grant JT (eds) *Surface analysis by Auger and X-ray photoelectron spectroscopy*. IM-Publications, Chichester, pp 295–343
35. Tougaard S (1990) *J Vac Sci Technol A* 8:2197–2203
36. Sato M, Tsukamoto N, Shiratori T, Furusawa T, Suzuki N, Tougaard S (2006) *Surf Interface Anal* 38:604–609
37. Simonsen AC, Pöhler JP, Jeynes C, Tougaard S (1999) *Surf Interface Anal* 27:52–56
38. Hansen HS, Tougaard S (1990) *Vacuum* 41:1710–1713
39. Jansson C, Tougaard S (1994) *J Vac Sci Technol A* 12:2332–2336
40. Yubero F, Jansson C, Batchelor DR, Tougaard S (1995) *Surf Sci* 331/333:753–758
41. Fujita D, Schleberger M, Tougaard S (1995) *Surf Sci* 331/333:343
42. Köver L, Tougaard S, Tóth J, Daróczy L, Szabó I, Langer G, Menyhard M (2001) *Surf Interface Anal* 31:271–279
43. Del Re M, Gouttebaron R, Dauchot JP, Leclere P, Lazzaroni R, Wautelet M, Hecq M (2002) *Surf Coatings Technol* 151–152:86–90
44. Schleberger M, Fujita D, Scharfschwerdt C, Tougaard S (1995) *J Vac Sci Technol B* 13:949–953
45. Schleberger M, Walsler P, Hunziker M, Landolt M (1999) *Phys Rev B* 60:14360–14365
46. Simonsen AC, Schleberger M, Tougaard S, Hansen JL, Larsen AN (1999) *Thin Solid Films* 338:165–171
47. Schleberger M, Simonsen AC, Tougaard S, Hansen JL, Larsen AN (1997) *J Vac Sci Technol A* 15:3032–3035
48. Simonsen AC, Tougaard S, Hansen JL, Larsen AN (1999) *Thin Solid Films* 338:165
49. Simonsen AC, Tougaard S, Hansen JL, Larsen AN (2001) *Surf Interface Anal* 31:328–337
50. Hansen HS, Bensaoula A, Tougaard S, Zborowski J, Ignatiev A (1992) *J Crystal Growth* 116:271–282
51. Sastry M, Sainkar SR (1993) *J Appl Phys* 73:767–770
52. Hansen HS, Tougaard S, Biebuyck H (1992) *J Electron Spectrosc Relat Phenom* 58:141
53. Suzuki N, Kato T, Tougaard S (2001) *Surf Interface Anal* 31:862–868
54. Andersen TH, Tougaard S, Larsen NB, Almdal K, Johannsen I (2001) *J Electron Spectrosc Relat Phenom* 121:93–110
55. Demoisson F, Raes M, Terryn H, Guillot J, Migeon HN, Reniers F (2008) *Surf Interface Anal* 40:566–570
56. Gallardo-Vega C, Cruz WDL, Tougaard S, Cota-Araiza L (2008) *Appl Surf Sci* 255:3000–3003
57. Hajati S, Zaporotchenko V, Faupel F, Tougaard S (2007) *Surf Sci* 601:3261–3267
58. Graat P, Somers MAJ (1998) *Surf Interface Anal* 26:773–782
59. Grosvenor AP, Kobe BA, McIntyre NS, Tougaard S, Lennard WN (2004) *Surf Interface Anal* 36:632–639
60. Grosvenor AP, Kobe BA, McIntyre NS (2004) *Surf Sci* 572:217–227
61. Tougaard S, Hetterich W, Nielsen AH, Hansen HS (1990) *Vacuum* 41:1583
62. Scharfschwerdt C, Kutscher J, Schneider F, Neumann M, Tougaard S (1992) *J Electron Spectrosc Relat Phenom* 60:321
63. Yubero F, González-Elipe AR, Tougaard S (2000) *Surf Sci* 457:24
64. Yubero F, Holgado JP, Barranco A, González-Elipe AR (2002) *Surf Interface Anal* 34:201–205
65. Semak BS, Jensen T, Tækker LB, Morgen P, Tougaard S (2002) *Surf Sci* 498:11
66. Jaime-Vasquez M, Martinka M, Jacobs RN, Benson JD (2007) *J Electronic Materials* 36:905–909
67. Fujita D, Schleberger M, Tougaard S (1996) *Surf Sci* 357/358:180
68. Fujita D, Schleberger M, Tougaard S (1996) *J Electron Spectrosc Relat Phenom* 82:173
69. Tougaard S, Braun W, Holub-krappe E, Saalfeld H (1988) *Surf Interface Anal* 13:225–227
70. Jansson C, Hansen HS, Jung C, Braun W, Tougaard S (1992) *Surf Interface Anal* 19:217
71. Graat P, Somers MAJ (1996) *Appl Surf Sci* 100/101:36–40
72. Lampimäki M, Lahtonen K, Jussila P, Hirsimäki M, Valden M (2007) *J Electron Spectrosc Relat Phenom* 154:69–78
73. Jussila P, Ali-Loytty K, Lahtonen K, Hirsimäki M, Valden M (2009) *Surf Sci* 603:3005–3010
74. Schleberger M (2000) *Surf Sci* 445:71–79
75. Jussila P, Lahtonen K, Lampimäki M, Hirsimäki M, Valden M (2008) *Surf Interface Anal* 40:1149–1156
76. Kisand V, Kikas A, Kukk E, Nömmiste E, Kooser K, Käambre T, Ruus R, Valden M, Hirsimäki M, Jussila P, Lampimäki M, Aksela H, Aksela S (2008) *J Phys Condens Matter* 20:145206, 9 pp
77. Preda I, Gutierrez A, Abbate M, Yubero F, Mendez J, Alvarez L, Soriano L (2008) *Phys Rev B* 77:075411, 7 pp
78. Dudeck D, Yanguas-Gil A, Yubero F, Cotrino J, Espinos JP, de la Cruz W, Gonzalez-Elipe AR (2007) *Surf Sci* 601:2223–2231
79. Mansilla C, Gracia F, Martin-Concepcion AI, Espinos JP, Holgado JP, Yubero F, Gonzalez-Elipe AR (2007) *Surf Interface Anal* 39:331–336
80. Martin-Concepcion AI, Yubero F, Espinos JP, Gonzalez-Elipe AR, Tougaard S (2003) *J Vac Sci Technol A* 21:1393
81. Reiche R, Oswald S, Yubero F, Espinos JP, Holgado JP, Gonzalez-Elipe AR (2004) *J Phys Chem B* 108:9905
82. Gracia F, Yubero F, Espinos JP, Gonzalez-Elipe AR (2005) *Appl Surf Sci* 252:189
83. Espinos JP, Martin-Concepcion AI, Mansilla C, Yubero F, Gonzalez-Elipe AR (2006) *J Vac Sci Technol A* 24:919
84. Mansilla C, Yubero F, Zier M, Reiche R, Oswald S, Holgado JP, Espinos JP, Gonzalez-Elipe AR (2006) *Surf Interface Anal* 38:510
85. Yubero F, Mansilla C, Ferrer FJ, Holgado JP, Gonzalez-Elipe AR (2007) *J Appl Phys* 101:124910, 6 pp
86. Lopez-Santos C, Yubero F, Cotrino J, Barranco A, Gonzalez-Elipe AR (2008) *J Phys D: Appl Phys* 41:225209, 12 pp
87. Tougaard S (1987) *J Vac Sci Technol A* 5:1275–1278
88. Johansson LS, Campbell JM, Koljonen K, Kleen M, Buchert J (2004) *Surf Interface Anal* 36:706
89. Idla K, Johansson LS, Campbell JM, Inganas O (2000) *Surf Interface Anal* 30:557–560
90. Perring M, Bowden NB (2008) *Langmuir* 24:10480–10487
91. Walton J, Fairley N (2005) *J Electron Spectrosc Relat Phenom* 148:29–40
92. Artyushkova K (2009) *J Electron Spectrosc Relat Phenom*. doi:10.1016/j.elspec.2009.05.014
93. Artyushkova K, Fulghum JE (2002) *Surf Interface Anal* 33:185–195
94. Peebles DE, Ohlhausen JA, Kotula PG, Hutton S, Blomfield C (2004) *J Vac Sci Technol A* 22:1579–1586
95. Vohrer U, Blomfield C, Page S, Roberts A (2005) *Appl Surf Sci* 252:61–65
96. Walton J, Fairley N (2004) *Surf Interface Anal* 36:89–91

97. Smith EF, Briggs D, Fairley N (2006) *Surf Interface Anal* 38:69–75
98. Payne BP, Grosvenor AP, Biesinger MC, Kobe BA, McIntyre NS (2007) *Surf Interface Anal* 39:582–592
99. Artyushkova K, Fulghum JE (2005) *J Electron Spectrosc Relat Phenom* 149:51–60
100. Tougaard S (2003) *J Vac Sci Technol A* 21:1081–1086
101. Tougaard S (2005) *J Vac Sci Technol A* 23:741–745
102. Hajati S, Coultas S, Blomfield C, Tougaard S (2006) *Surf Sci* 600:3015–3021
103. Hajati S, Coultas S, Blomfield C, Tougaard S (2008) *Surf Interface Anal* 40:688–691
104. Hajati S, Tougaard S, Walton J, Fairley N (2008) *Surf Sci* 602:3064–3070
105. Escher M, Winkler K, Renault O, Barrett N (2009) *J Electron Spectrosc Relat Phenom*. doi:10.1016/j.elspec.2009.06.001
106. Liu ZC, Zhang X, He NY, Lu ZH, Chen ZC (2009) *Colloids Surf B: Biointerfaces* 71:238–242
107. Baer DR, Engelhard MH (2008) *J Electron Spectrosc Relat Phenom*. doi:10.1016/j.elspec.2009.09.003